

Surface effects on the red giant branch

W. H. Ball,^{1,2*} N. Themeßl^{3,2,4} and S. Hekker^{3,2}

¹*School of Physics and Astronomy, University of Birmingham, Edgbaston, Birmingham B15 2TT, United Kingdom*

²*Stellar Astrophysics Centre, Department of Physics and Astronomy, Aarhus University, Ny Munkegade 120, DK-8000 Aarhus C, Denmark*

³*Max-Planck-Institut für Sonnensystemforschung, Justus-von-Liebig-Weg 3, D-37077 Göttingen, Germany*

⁴*Institut für Astrophysik, Georg-August-Universität Göttingen, Friedrich-Hund-Platz 1, 37077 Göttingen, Germany*

Accepted XXX. Received YYY; in original form ZZZ

ABSTRACT

Individual mode frequencies have been detected in thousands of individual solar-like oscillators on the red giant branch (RGB). Fitting stellar models to these mode frequencies, however, is more difficult than in main-sequence stars. This is partly because of the uncertain magnitude of the surface effect: the systematic difference between observed and modelled frequencies caused by poor modelling of the near-surface layers. We aim to study the magnitude of the surface effect in RGB stars. Surface effect corrections used for main-sequence targets are potentially large enough to put the non-radial mixed modes in RGB stars out of order, which is unphysical. Unless this can be circumvented, model-fitting of evolved RGB stars is restricted to the radial modes, which reduces the number of available modes. Here, we present a method to suppress gravity modes (g-modes) in the cores of our stellar models, so that they have only pure pressure modes (p-modes). We show that the method gives unbiased results and apply it to three RGB solar-like oscillators in double-lined eclipsing binaries: KIC 8410637, KIC 9540226 and KIC 5640750. In all three stars, the surface effect decreases the model frequencies consistently by about 0.1–0.3 μHz at the frequency of maximum oscillation power ν_{max} , which agrees with existing predictions from three-dimensional radiation hydrodynamics simulations. Though our method in essence discards information about the stellar cores, it provides a useful step forward in understanding the surface effect in RGB stars.

Key words: binaries: eclipsing – stars: interiors – stars: evolution – stars: oscillations – stars: individual: KIC 8410637, KIC 9540226, KIC 5640750

1 INTRODUCTION

Long-term space-based monitoring—principally from CoRoT (Auv^{ergne et al. 2009}) and *Kepler* (Borucki et al. 2010)—has led to the detection of oscillation mode frequencies in thousands of solar-like oscillators. Most of these solar-like oscillators are in the helium core-burning red clump (RC) or on the hydrogen shell-burning red giant branch (RGB), where their oscillations are slower (and therefore detectable at longer cadences), and many major advances and discoveries have been made using these data (see e.g. Hekker & Christensen-Dalsgaard 2017, for a review). An early breakthrough was in the use of the period spacing between dipole mixed modes to distinguish RC stars from RGB stars, even when their non-seismic observables (e.g. surface gravity $\log g$ and effective temperature T_{eff}) make them hard to tell apart (Beck et al. 2011; Bedding et al. 2011). This analysis is now common, and has been used to identify smaller subgroups, including stars in the secondary clump or potentially going through the helium flash (Mosser et al. 2014). A second major discovery has been the measurement of core rotation rates in subgiants and red giants (Beck et al. 2012; Deheuvels et al. 2012).

These core rotation rates are slower than current models predict (e.g. Marques et al. 2013) and have sparked research into other mechanisms that could transport angular momentum between the core and envelope (e.g. Belkacem et al. 2015b,a). Finally, given that they can be seen at distances of thousands of parsecs, red giants have contributed to multiple results in the field of galactic archaeology (e.g. Miglio et al. 2013).

Despite the progress outlined above, there has been less success in fitting stellar models directly to the observed mode frequencies, as is now relatively routine for main-sequence solar-like oscillators (e.g. Appourchaux et al. 2015; White et al. 2017; Silva Aguirre et al. 2017; Creevey et al. 2017). This is partly because red giants take more time to model: the evolutionary tracks must evolve further, the evolutionary computations become slower, and the dense spectrum of non-radial modes takes much longer to compute, though some progress is being made. Pérez Hernández et al. (2016) fit stellar models to the frequencies measured by Corsaro et al. (2015) by using the period spacing between dipole ($\ell = 1$) mixed modes and the individual mode frequencies for the radial, quadrupole and octupole modes ($\ell = 0, 2, 3$). More recently, Li et al. (2018) fit stellar models to a sample of red giants in eclipsing binaries using the stellar models to guide the identification of mode frequencies in the observations.

* E-mail: wball@bison.ph.bham.ac.uk

In addition to the slower computation, there is the problem of the ‘surface effect’: the systematic difference between observed and modelled frequencies caused by poor modelling of the near-surface layers (see [Ball 2017](#), for a recent review). The effect is well-known in the Sun whereas it is hard to know what to expect in red giants. [Sonoji et al. \(2015\)](#) computed the frequency shifts caused by replacing the near-surface layers of stellar models—including a red giant—but restricted the calculation to radial modes.

For non-radial modes, the frequency shifts are potentially larger than the observed period spacings between the many mixed modes, in which case the parametrisations used for dwarfs would imply an unphysical breaking of the ordering of the modes. If all neighbouring modes were shifted by similar amounts (as is in dwarf solar-like oscillators), this would not be a problem. For mixed modes, however, we expect the surface effect to be greater in those with a stronger p-mode component. This can mean that two neighbouring modes are shifted by very different amounts (see [Sec. 2.3](#) and [Fig. 2](#)). What we really expect is that the p-mode component is shifted by the surface effect and the shifted p-mode couples to a different g-mode in the core. Our study of the surface effect would still be possible if we restrict our attention to radial modes only, for which mixed modes are not possible. This, however, would come at the cost of discarding about two thirds of our observed p-dominated mode frequencies and reduce the precision of our parameters. A simplistic calculation using the results presented here suggests that our derived uncertainties would be roughly 70 per cent larger if we only used the radial mode frequencies.

To exploit the non-radial mode frequencies, we isolate the p-mode components of the mixed modes by suppressing the g-mode oscillations. We achieve this by setting the squared Brunt–Väisälä frequency N^2 to zero throughout the convectively-stable core (see [Sec. 2.3](#) for details). We note that this is one of several ways to extract “pure” p-mode frequencies. For example, one alternative is to restrict the oscillation calculation for the non-radial modes to the convective envelope. We have chosen to set N^2 to zero because it is straightforward to implement.¹

The complementary information available for stars in binary systems makes them ideal targets for constraining stellar physics. In particular, double-lined eclipsing binaries (DEBs) allow independent measurements of the masses and radii of the components. There are few main-sequence solar-like oscillators in binaries, as predicted by [Miglio et al. \(2014\)](#). Given their greater number, we expect more binaries containing RGB or RC stars, though usually only one component will have measurable oscillations. Nearly 20 such systems are now known and they have been used to study potential biases in the asteroseismic scaling relations (e.g. [Gaulme et al. 2016](#); [Themeßl et al. 2018](#), and references therein).

Here, we fit stellar models to mode frequencies measured for the RGB stars in three DEBs, with the aim of investigating whether the surface corrections used for main-sequence solar-oscillators are still valid and agree with our expectations. As a secondary result, we also compare the stellar parameters that are recovered with those found from dynamical modelling of the binary system.

2 OBSERVATIONS, MODELS AND FITTING METHOD

2.1 Target stars

Our asteroseismic targets are the three red giants KIC 8410637, KIC 9540226 and KIC 5640750, hereafter referred to as stars A, B and C, observed by *Kepler* during its nominal mission. Power spectra for the three stars are shown in [Fig. 1](#) and their basic stellar parameters and orbital parameters (from [Themeßl et al. 2018](#)) are listed in [Tables 1](#) and [2](#). All three stars have been identified as RGB stars and are parts of detached, eclipsing, spectroscopic binary systems that have been studied since their respective discoveries. Star A was the first oscillating red giant detected in an eclipsing binary ([Hekker et al. 2010](#)). [Frandsen et al. \(2013\)](#) subsequently obtained high resolution spectroscopy from which they measured the masses and radii of both components. [Beck et al. \(2014\)](#) analysed a sample of 18 red giants in eccentric binary systems, including star B. [Brogaard et al. \(2016\)](#) also analysed stars A and B. All three stars were part of the ensembles studied by [Gaulme et al. \(2013, 2014\)](#), and [Gaulme et al. \(2016\)](#) included stars A and B in their comparison of dynamical and asteroseismic masses.

The data used here are from [Themeßl et al. \(2018\)](#), who measured the oscillation frequencies of stars A, B and C, as well as computing updated orbital solutions to the light curves and radial velocities. They compared the masses and radii from the orbital solutions with those produced by asteroseismic scaling relations ([Brown et al. 1991](#); [Kjeldsen & Bedding 1995](#)) and grid-based modelling, and found that the results agree if the scaling relations are corrected for variations with mass, temperature, metallicity and surface effects. [Themeßl et al. \(2018\)](#) report two masses and radii for star C derived from the eclipse and radial velocity observations. The two orbital solutions are of similar quality, with the ambiguity principally caused by poor coverage of the radial velocity observations as a function of orbital phase. We initially considered both solutions and, like [Themeßl et al. \(2018\)](#), concluded that the lower-mass solution was consistent with our seismic results for the other two stars. To avoid confusion, we hereafter restrict our attention to the lower-mass orbital solution for star C.

2.2 Stellar models

We computed stellar models using the Modules for Experiments in Stellar Astrophysics (MESA², revision 9575, [Paxton et al. 2011, 2013, 2015](#)). Opacities at high and low temperatures are taken from the tables by the OPAL collaboration ([Iglesias & Rogers 1996](#)) and [Ferguson et al. \(2005\)](#), respectively. Nuclear reaction rates are drawn either from the NACRE tables ([Angulo et al. 1999](#)) or, if a given rate was not available there, from the tables by [Caughlan & Fowler \(1988\)](#). For the specific reactions $^{14}\text{N}(p, \gamma)^{15}\text{O}$ and $^{12}\text{C}(\alpha, \gamma)^{16}\text{O}$, we use the revised rates by [Imbriani et al. \(2005\)](#) and [Kunz et al. \(2002\)](#). Convection is described by mixing-length theory ([Böhm-Vitense 1958](#)) as derived in [Cox & Giuli \(1968\)](#) with no overshooting. For the solar abundances, we use the overall abundance and mixture given by [Grevesse & Sauval \(1998\)](#). For the surface boundary condition, we extended the outermost meshpoint of the stellar model to an optical depth of $\tau = 10^{-4}$, which in effect creates a grey Eddington atmosphere that is included in the interior model. Photospheric values are determined by interpolating at the photospheric optical depth $\tau = 2/3$.

¹ Our implementation in MESA requires 13 lines of additional code (see [Appendix A](#)).

² <http://mesa.sourceforge.net>

Table 1. Table of stars' observed properties, taken from [Themeßl et al. \(2018\)](#).

| Star | KIC | T_{eff}/K | $[\text{Fe}/\text{H}]$ | $v_{\text{max}}/\mu\text{Hz}$ | $\Delta v/\mu\text{Hz}$ | M/M_{\odot} | R/R_{\odot} |
|------|---------|---------------------------|------------------------|-------------------------------|-------------------------|-------------------|--------------------|
| A | 8410637 | 4605 ± 80 | 0.02 ± 0.08 | 46.4 ± 0.3 | 4.564 ± 0.004 | 1.472 ± 0.017 | 10.596 ± 0.049 |
| B | 9540226 | 4585 ± 75 | -0.31 ± 0.09 | 26.7 ± 0.2 | 3.153 ± 0.006 | 1.390 ± 0.031 | 13.43 ± 0.17 |
| C | 5640750 | 4525 ± 75 | -0.29 ± 0.09 | 24.1 ± 0.2 | 2.969 ± 0.006 | 1.158 ± 0.014 | 13.119 ± 0.090 |

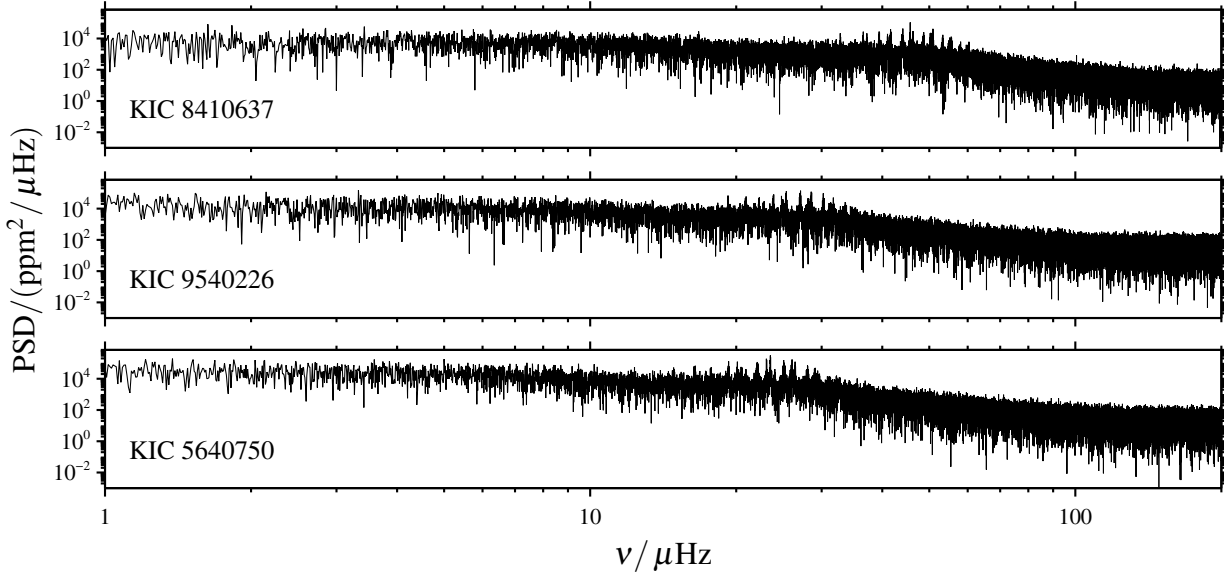

Figure 1. Power density spectra of KIC 8410637 (star A, top), KIC 9540226 (star B, middle) and KIC 5640750 (star C, bottom).

Table 2. Table of stars' orbital properties, taken from [Themeßl et al. \(2018\)](#).

| Star | P/d | e | q |
|------|-----------------------|-------------------|-------------------|
| A | 408.3248 ± 0.0004 | 0.694 ± 0.004 | 0.890 ± 0.005 |
| B | 175.4438 ± 0.0008 | 0.387 ± 0.003 | 0.730 ± 0.032 |
| C | 987.398 ± 0.006 | 0.322 ± 0.008 | 0.971 ± 0.012 |

We note that our models omit the effects of gravitational settling, radiative levitation and rotation. The three stars here are massive enough that the current implementation of gravitational settling would completely drain the surface of helium and metals during the main sequence evolution, which we regard as less justified than omitting gravitational settling. In MESA, calculations including radiative levitation are presently too time-consuming and rotation is only implemented in the diffusion approximation, so we omit them here. Mode frequencies were computed using the Aarhus adiabatic pulsation code (ADIPLS, [Christensen-Dalsgaard 2008](#)) without remeshing.

2.3 Suppressing mixed modes

As a solar-like oscillator evolves up the red giant branch, so its spectrum of mixed modes becomes more closely spaced. Eventually, the surface corrections are potentially larger than the observed spacing between g-modes, in which case the corrections that are used for dwarfs and subgiants will break down. This phenomenon is demonstrated in Fig. 2, which shows mode inertiae \mathcal{I} as a function of frequency for the model used as a hare for KIC 8410637 (see

Sec. 2.3).³ The black curve shows the inertiae of the unmodified stellar model. The blue curve shows the inertiae in the same model after the mode frequencies have been shifted by introducing a sound speed perturbation concentrated at the stellar surface. Specifically, we modified the first adiabatic index Γ_1 by assigning it a new value

$$\Gamma_1' = \Gamma_1 \cdot \left(1 - 0.4 e^{-10^6[(r/R)-1]^2}\right) \quad (1)$$

though any sharp peak at the stellar surface will produce a similar effect. Here, r is the radial co-ordinate in the stellar model and R is the photospheric radius. The frequencies and mode inertiae are changed such that a different mode is now identified as the most p-dominated (i.e. the mode with the lowest inertia, see blue curve). The orange curve shows the original mode frequencies but now corrected using the cubic correction by [Ball & Gizon \(2014\)](#) so that the frequency of the most p-dominated mode matches that of the modified model. The size of the surface correction applied to match the black mode to the blue is so large that it disrupts the monotonic relationship between radial order and mode frequency (see orange curve).

To address this problem, we note that the observed frequencies of the three red giants in binary systems contain one mode per acoustic radial order and per angular degree ([Themeßl et al. 2018](#)). This is always true for radial modes and in these observations it is also true for the non-radial modes, even though many mixed modes are theoretically present. The observed non-radial modes are

³ The figure follows the example discussed by [Li et al. \(2018, Sec. 4.2\)](#) and shown in their Figs 3 and 4.

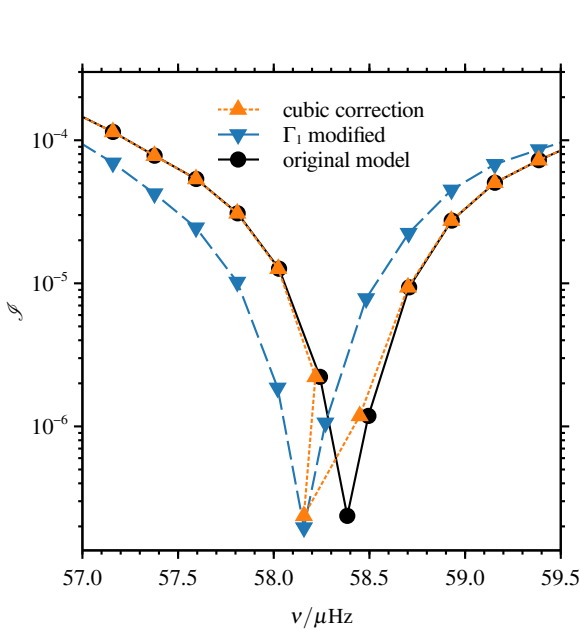


Figure 2. Mode inertia as a function of frequency for the stellar model used as a hare for KIC 8410637 (see the end of this section). The solid black curve shows the values for the unmodified model, the dashed blue curve for a model in which the first adiabatic index Γ_1 has been decreased near the surface, and the dotted orange curve the original values with a cubic surface correction applied to try to match the mode with the lowest inertia in the modified model (blue). In the corrected frequencies (orange), the correction is large enough to change the order of the modes with frequency.

those with the largest amplitudes and presumably the lowest inertias, which implies that they are also the least mixed. If there were no mode mixing, there would be only one “pure” p-mode per acoustic radial order and per angular degree. To proceed, we therefore assume that the observed modes are those whose frequencies are closest to these hypothetical pure p-modes, and we modify the stellar models to compute the frequencies of these pure p-modes. We describe these modifications here and provide the Fortran source code in Appendix A.

We suppress g-modes in the core of the star by setting the square of the Brunt–Väisälä frequency N to zero in the convectively-stable regions beneath the convective envelope, i.e. we assign $N^2 = 0$ wherever $N^2 > 0$ in the core. In practice, we use the dimensionless square of the Brunt–Väisälä frequency \mathcal{A}^4 , which is defined by

$$\mathcal{A} = \frac{r}{g} N^2 = \frac{1}{\Gamma_1} \frac{d \ln P}{d \ln r} - \frac{d \ln \rho}{d \ln r} \quad (2)$$

where r is the radial co-ordinate, g the gravity, Γ_1 the first adiabatic index, P the pressure and ρ the density in the unmodified stellar model.

We modify the stellar model by setting the dimensionless square of the Brunt–Väisälä frequency to a new value $\mathcal{A}' = 0$ wherever $\mathcal{A} > 0$ in the core. We do not wish to change the pressure or density, so to keep the model consistent with the definition above

⁴ This is sometimes referred to as the *Ledoux discriminant* or *convective parameter*.

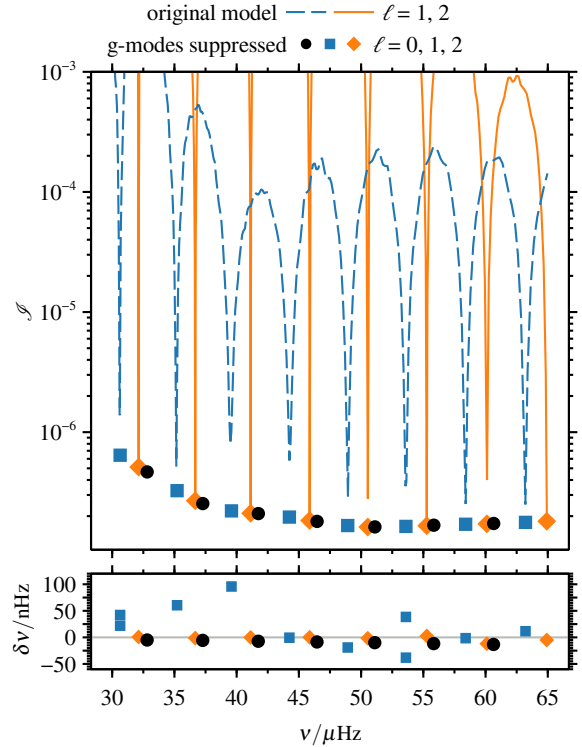


Figure 3. Demonstration of the effect of suppressing g-mode oscillations, as described in Sec. 2.3, in the model of star A (KIC 8410637) that served as the hare. In the upper panel, the dashed blue and solid orange lines show the mode inertias as a function of frequency for the $\ell = 1$ and 2 modes before the g-modes were suppressed. The black circles, blue squares and orange diamonds show the $\ell = 0, 1$ and 2 modes after the g-modes are suppressed. The lower panel shows the differences between the mode frequencies before and after the g-modes are suppressed. The symbols are as in the upper panel. For the non-radial modes the differences are shown relative to modes with the lowest inertia for each radial order in the unmodified model. For two dipole modes (at 30.6 and $53.6 \mu\text{Hz}$), there is another mode with an inertia within 10 per cent of the lowest, which we have also shown.

we must change the first adiabatic index to

$$\Gamma_1' = \frac{d \ln P / d \ln r}{d \ln \rho / d \ln r} \quad (3)$$

Thus, during the model-fitting, we change \mathcal{A} to \mathcal{A}' and Γ_1 to Γ_1' in the stellar models before they are loaded by the oscillation code.

As a practical point, rather than recompute the radial derivatives above from finite differences, we use existing information in the stellar model. The pressure gradient is known from the equation of hydrostatic equilibrium,

$$\frac{dP}{dr} = -\rho g \quad (4)$$

and the density gradient is provided by the Brunt–Väisälä frequency before the stellar model is modified. i.e.

$$\frac{d\rho}{dr} = \frac{1}{\Gamma_1} \frac{d \ln P}{d \ln r} - \mathcal{A} \quad (5)$$

where we emphasize that all the variables are from the unmodified stellar model. Fig. 3 shows the resulting change in the mode frequencies and inertias in a model of star A. The upper panel shows that the mode frequencies after modifying the model occur at the minima of the mode inertias, where we expect the pure p-modes

would occur. The lower panel shows the differences in the mode frequencies before and after modification. The frequency differences for the radial modes should theoretically be zero. We have modified Γ_1 , which affects the radial modes, but the frequencies change by less than $0.015 \mu\text{Hz}$, which is negligible.

To validate the mode suppression method described above, we performed a simple hare and hounds exercise using a model of star A produced by an early iteration of our model-fitting routine. We computed the full frequency spectrum of the stellar model (the hare) and then selected the same modes as the observations. For the non-radial modes, we used the modes with the lowest mode inertiae, which gave one mode per angular degree and radial order. We perturbed these mode frequencies (and the non-seismic data) by random variates drawn from normal distributions with the observed variances and then found a best-fitting model (the hound) using the mode suppression described above.

The first two rows of Tables 3 and 4 give the parameters of the target model (the hare) and the best-fitting model (the hound). The hound clearly recovers the properties of the hare within the uncertainties, which demonstrates that the mode suppression method does not bias our results.

2.4 Model-fitting procedure

We fit the stellar models to the observed data using essentially the same method as in Ball & Gizon (2017). We minimised the total χ^2 , defined by

$$\chi^2 = \sum_{i=1}^{N_{\text{obs}}} \left(\frac{y_{\text{obs},i} - y_{\text{mdl},i}}{\sigma_i} \right)^2 \quad (6)$$

where $y_{\text{obs},i}$, $y_{\text{mdl},i}$ and σ_i are the observed value, modelled value and observed uncertainty of the i -th observable, of which there are N_{obs} in total. The observables are the effective temperature T_{eff} , surface metallicity $[\text{Fe}/\text{H}]_s$ and the individual mode frequencies. For each star, we also recomputed χ^2 including the dynamical mass M and radius R as constraints.

To correct for the surface effect, we used either the one-term (cubic) or two-term (combined) corrections by Ball & Gizon (2014). These fit the differences between the modelled and observed frequencies $\delta v_i = v_{\text{obs},i} - v_{\text{mdl},i}$ with the formulae

$$\delta v_i = a_3 (v_{\text{mdl},i}/v_{\text{ac}})^3 / \mathcal{I}_i \quad (7)$$

or

$$\delta v_i = (a_{-1} (v_{\text{mdl},i}/v_{\text{ac}})^{-1} + a_3 (v_{\text{mdl},i}/v_{\text{ac}})^3) / \mathcal{I}_i \quad (8)$$

for the one- or two-term correction, respectively. Here, v_{ac} is the acoustic cut-off frequency, used to non-dimensionalise the equations. For convenience, it is computed using the scaling relation

$$\frac{v_{\text{ac}}}{v_{\text{ac},\odot}} = \frac{g}{g_{\odot}} \left(\frac{T_{\text{eff}}}{T_{\text{eff},\odot}} \right)^{-1/2} \quad (9)$$

and we use $v_{\text{ac},\odot} = 5000 \mu\text{Hz}$, $\log g_{\odot} = 4.438$ and $T_{\text{eff},\odot} = 5777 \text{K}$. The best-fitting values of the coefficients a_{-1} and a_3 are found by linear regression using all the observed modes. We used the one-term (cubic) correction (eq. 7) unless otherwise noted.

We created a handful of initial guesses for each star using the scaling relations and then proceeded with an iterative method. For each choice of mass M , initial helium abundance Y_0 , initial metallicity $[\text{Fe}/\text{H}]_0$ and mixing-length parameter α , we started an evolutionary track from a chemically-homogeneous pre-main-sequence

model with central temperature $9 \times 10^5 \text{K}$. The timestep was gradually reduced to a minimum of $10^{4.5} \text{yr}$ as the stellar model first matched the spectroscopic parameters and then the radial mode frequencies. Once these requirements were met, the full set of mode frequencies was computed (using the mode suppression method) and the total χ^2 recorded. The parameters for each model with $\chi^2 < 2000$ were stored. As described in more detail below, we found best-fitting models both before and after the RGB bump: the brief decrease in luminosity as the hydrogen-burning shell passes through the composition discontinuity left by the convective envelope at its maximum depth. We used the full sequence of models with $\chi^2 < 2000$ to identify the best-fitting models for each case separately.

We then iterated on the parameters of the best-fitting models—separately for the pre- and post-bump models—principally using the Nelder–Mead downhill simplex method (Nelder & Mead 1965). When the downhill simplex fails, it usually resorts to shrinking the entire simplex towards the current best-fitting model. To avoid this, we tried to produce better-fitting models using a variety of methods, including: linear extrapolations from subsets of the sample so far; uniformly-distributed models with the 1 to 3σ confidence regions; extensions of lines between selected pairs of models; and reflections across the best fitting model. This process, though somewhat haphazard, is aimed at preventing convergence on a local minimum. The search for better models ended when several dozen attempts failed to reduce the best χ^2 by more than one.

We determined uncertainties of the model parameters (i.e. the parameters in Table 3, which define the stellar models) from ellipsoids bounding surfaces of constant χ^2 , in particular by finding the ellipsoids that would simultaneously enclose all the parameters of all models within an ellipsoid corresponding to that value of χ^2 . That is, if the minimum of χ^2 was χ_0^2 , we required that models with $\chi^2 = \chi_0^2 + 1$ and $\chi_0^2 + 4$ are simultaneously contained within the 1σ and 2σ ellipsoids. Uncertainties for derived quantities (i.e. the quantities given in Table 4, which are derived from the stellar models) were derived by calculating a linear fit to each derived property with respect to the model parameters and propagating the uncertainties linearly.

The method above describes our fiducial fits, denoted ‘‘Fid.’’ in Tables 3, 4 and 5. We also performed a second set of fits using the two-term surface correction proposed by Ball & Gizon (2014), denoted ‘‘BG14-2’’ (eq. 8); a third set in which the mixing-length parameter was fixed to the solar-calibrated value of $\alpha_{\odot} = 1.66$, denoted ‘‘ α_{\odot} ’’; and a fourth set in which the dynamical masses and radii were included as observational constraints, denoted ‘‘MR’’.

3 RESULTS

3.1 Overview

The best-fitting model parameters are presented in Tables 3 and 4. Table 3 provides the model parameters that specify the stellar model while Table 4 provides other observable and derived quantities. Each row specifies which of the four fits is given and the final ‘‘pre’’ or ‘‘post’’ indicates whether that fit is for models before or after the RGB bump. Figs 4–6 show the differences between the observed and modelled frequencies for each star before and after the surface effects have been corrected, with error bars indicating the observed uncertainties. In each figure, the four fits appear in different panels with the same x - and y -axes. We have also indicated the surface correction predicted by eq. (10) of Sonoi et al. (2015).

Table 3. Model parameters for the various model fits. The first two rows give the hare and hound by which we tested our g-mode suppression method for bias (see Sec. 2.3). The remaining rows are eight fits for each of stars A, B and C, as described in Sec. 2.4. The first columns specify the runs as described in Sec. 2.4, grouped by star (A, B or C). The remaining columns give the mass, initial helium abundance, initial metallicity, mixing-length parameter, age and surface term coefficients for each fit.

| Star | Run | M/M_{\odot} | Y_0 | $[\text{Fe}/\text{H}]_0$ | α | t/Gyr | $a_3/10^{-6} \mu\text{Hz}$ | $a_{-1}/10^{-7} \mu\text{Hz}$ |
|-------|-------------------------|-------------------|-------------------|--------------------------|-----------------|-----------------|----------------------------|-------------------------------|
| Hare | | 1.723 | 0.238 | 0.147 | 2.29 | 2.42 | 0 | |
| Hound | Fid., pre | 1.771 ± 0.098 | 0.207 ± 0.040 | 0.031 ± 0.138 | 2.14 ± 0.15 | 2.39 ± 0.27 | -0.22 ± 0.26 | |
| A | Fid., pre | 1.671 ± 0.067 | 0.216 ± 0.024 | 0.069 ± 0.065 | 2.12 ± 0.15 | 2.88 ± 0.27 | -1.67 ± 0.40 | |
| | Fid., post | 1.694 ± 0.071 | 0.213 ± 0.022 | 0.058 ± 0.074 | 2.09 ± 0.16 | 2.78 ± 0.31 | -1.76 ± 0.42 | |
| | BG14-2, pre | 1.732 ± 0.083 | 0.208 ± 0.023 | 0.075 ± 0.064 | 2.01 ± 0.15 | 2.71 ± 0.28 | -2.46 ± 0.51 | -3.40 ± 0.56 |
| | BG14-2, post | 1.761 ± 0.083 | 0.202 ± 0.026 | 0.059 ± 0.085 | 1.95 ± 0.17 | 2.64 ± 0.29 | -2.73 ± 0.62 | -3.48 ± 0.79 |
| | α_{\odot} , pre | 1.700 ± 0.080 | 0.187 ± 0.027 | 0.075 ± 0.074 | 1.66 ± 0.00 | 3.35 ± 0.30 | -3.05 ± 0.27 | |
| | α_{\odot} , post | 1.731 ± 0.077 | 0.185 ± 0.024 | 0.025 ± 0.084 | 1.66 ± 0.00 | 3.01 ± 0.32 | -3.20 ± 0.24 | |
| | MR, pre | 1.495 ± 0.017 | 0.269 ± 0.012 | 0.204 ± 0.062 | 2.17 ± 0.17 | 3.41 ± 0.31 | -1.82 ± 0.35 | |
| | MR, post | 1.497 ± 0.018 | 0.271 ± 0.012 | 0.213 ± 0.053 | 2.18 ± 0.21 | 3.39 ± 0.23 | -1.87 ± 0.45 | |
| B | Fid., pre | 1.549 ± 0.073 | 0.200 ± 0.023 | -0.361 ± 0.072 | 1.74 ± 0.11 | 2.78 ± 0.28 | -6.23 ± 0.86 | |
| | Fid., post | 1.593 ± 0.076 | 0.175 ± 0.027 | -0.257 ± 0.100 | 1.90 ± 0.18 | 3.26 ± 0.50 | -4.30 ± 1.49 | |
| | BG14-2, pre | 1.559 ± 0.075 | 0.202 ± 0.026 | -0.322 ± 0.075 | 1.71 ± 0.13 | 2.78 ± 0.31 | -8.04 ± 1.42 | -7.45 ± 2.72 |
| | BG14-2, post | 1.596 ± 0.080 | 0.185 ± 0.030 | -0.282 ± 0.112 | 1.80 ± 0.20 | 2.98 ± 0.48 | -6.68 ± 2.28 | -5.93 ± 2.24 |
| | α_{\odot} , pre | 1.562 ± 0.077 | 0.193 ± 0.022 | -0.348 ± 0.067 | 1.66 ± 0.00 | 2.86 ± 0.27 | -6.72 ± 0.62 | |
| | α_{\odot} , post | 1.615 ± 0.080 | 0.169 ± 0.031 | -0.319 ± 0.101 | 1.66 ± 0.00 | 3.06 ± 0.43 | -6.25 ± 0.68 | |
| | MR, pre | 1.439 ± 0.034 | 0.234 ± 0.015 | -0.294 ± 0.053 | 1.80 ± 0.09 | 3.03 ± 0.19 | -6.30 ± 0.85 | |
| | MR, post | 1.443 ± 0.029 | 0.225 ± 0.017 | -0.163 ± 0.094 | 1.95 ± 0.16 | 3.67 ± 0.66 | -4.62 ± 1.39 | |
| C | Fid., pre | 1.270 ± 0.064 | 0.222 ± 0.027 | -0.486 ± 0.100 | 1.68 ± 0.09 | 4.38 ± 0.41 | -7.75 ± 1.05 | |
| | Fid., post | 1.379 ± 0.064 | 0.143 ± 0.040 | -0.253 ± 0.125 | 1.89 ± 0.18 | 6.79 ± 1.43 | -3.61 ± 1.94 | |
| | BG14-2, pre | 1.313 ± 0.061 | 0.211 ± 0.026 | -0.432 ± 0.107 | 1.57 ± 0.13 | 4.38 ± 0.44 | -10.77 ± 2.05 | -9.17 ± 2.97 |
| | BG14-2, post | 1.369 ± 0.072 | 0.164 ± 0.041 | -0.301 ± 0.117 | 1.78 ± 0.18 | 5.76 ± 1.09 | -6.17 ± 2.70 | -4.58 ± 2.27 |
| | α_{\odot} , pre | 1.277 ± 0.048 | 0.215 ± 0.017 | -0.499 ± 0.065 | 1.66 ± 0.00 | 4.46 ± 0.34 | -7.93 ± 0.76 | |
| | α_{\odot} , post | 1.384 ± 0.062 | 0.142 ± 0.036 | -0.314 ± 0.092 | 1.66 ± 0.00 | 6.34 ± 1.13 | -5.61 ± 0.86 | |
| | MR, pre | 1.179 ± 0.011 | 0.257 ± 0.012 | -0.369 ± 0.071 | 1.63 ± 0.11 | 4.95 ± 0.27 | -8.41 ± 1.10 | |
| | MR, post | 1.180 ± 0.014 | 0.243 ± 0.019 | -0.175 ± 0.118 | 1.86 ± 0.18 | 6.58 ± 1.21 | -5.37 ± 1.76 | |

The first point the reader may notice in Tables 3 and 4 is that the uncertainties are larger than often quoted in the asteroseismology of dwarf solar-like oscillators—especially Sun-like stars—when individual frequencies are available (e.g. Reese et al. 2016; Silva Aguirre et al. 2017; Bellinger et al. 2017). Our uncertainties are also larger than those given for the slightly less evolved red giants ($\log g \approx 3$) studied by Pérez Hernández et al. (2016). Though our uncertainties on the radii are around the 2 per cent level, our uncertainties on the masses can be nearly 6 per cent. This is at least in part because our suppression of g-modes in the core discards a great deal of information about the stellar interior. For example, we cannot possibly have the diagnostic power of the period spacing that has been demonstrated by Mosser et al. (2014). We are, however, still able to tightly constrain the mean density and surface gravity, and we achieve age uncertainties of about 10 to 20 per cent. Above all, we are still able to make useful inferences about the surface effects, which are our main interests here.

We also note that the fits that are not constrained by the orbital solution (i.e. run MR) have initial helium abundances Y_0 that are smaller—sometimes significantly—than the primordial value of $0.249^{+0.025}_{-0.026}$ (Planck Collaboration et al. 2016).

3.2 Two solutions

As mentioned above, for most choices of initial model parameters we found similarly good models both before and after the RGB bump. In both cases, the star is ascending the giant branch. i.e. the luminosity is increasing and the effective temperature decreasing. For some

tracks the code recorded models during the RGB bump (when the luminosity decreases and the effective temperature increases) but such models always provided much poorer fits, unlike the pre- and post-bump models we report. In stars A and B the two models are of similar quality, though in star C the post-bump model appears to fit the data slightly better.

The occurrence of two solutions is presumably also a consequence of suppressing the g-modes in the core. For a given choice of initial parameters, both models will have similar p-mode qualities like surface gravity and mean density, and hence only a modest difference in their p-mode spectra. The full models should differ in their g-mode spectra but we have in effect discarded this information.

The existence of the two solutions does not undermine the quantitative results. In stars A and B, all of the pre- and post-bump fits are consistent within uncertainties, even for the mean densities $\bar{\rho}$ and surface gravities $\log g$, which have small uncertainties. This is not so for star C and, given that the post-bump models fit better in most cases, we conclude that star C has evolved past the RGB bump.

3.3 Comparison with binary solutions

In Fig. 7, we compare the masses, radii, mean densities and surface gravities of the three stars with the results obtained from the orbital solutions of the three stars. Without constraining the masses and radii to match the values found in the orbital solutions, the models generally disagree with the orbital parameters at roughly the 2 to 3σ level.

Table 4. The derived stellar parameters for the model fits, as labelled in Table 3. The columns are the radius, mean density, surface gravity, surface metallicity, effective temperature, luminosity and χ^2 per degree of freedom.

| Star | Run | R/R_\odot | $\bar{\rho}/(10^{-3}\bar{\rho}_\odot)$ | $\log g$ | $[\text{Fe}/\text{H}]_s$ | T_{eff}/K | $\log L/L_\odot$ | χ^2_{red} |
|-------|-----------------------|--------------------|--|-------------------|--------------------------|---------------------------|-------------------|-----------------------|
| Hare | | 11.113 | 1.255 | 2.578 | 0.160 | 4792 | 1.771 | |
| Hound | Fid., pre | 11.218 ± 0.220 | 1.255 ± 0.004 | 2.582 ± 0.007 | 0.045 ± 0.137 | 4751 ± 88 | 1.765 ± 0.038 | 1.87 |
| | Fid., pre | 11.002 ± 0.155 | 1.254 ± 0.003 | 2.574 ± 0.005 | 0.084 ± 0.065 | 4708 ± 92 | 1.732 ± 0.035 | 3.31 |
| | Fid., post | 11.064 ± 0.165 | 1.251 ± 0.003 | 2.575 ± 0.005 | 0.072 ± 0.074 | 4704 ± 89 | 1.736 ± 0.034 | 3.31 |
| | BG14-2, pre | 11.099 ± 0.184 | 1.267 ± 0.003 | 2.582 ± 0.006 | 0.089 ± 0.063 | 4648 ± 88 | 1.717 ± 0.035 | 2.45 |
| A | BG14-2, post | 11.170 ± 0.183 | 1.263 ± 0.004 | 2.583 ± 0.006 | 0.074 ± 0.085 | 4622 ± 98 | 1.713 ± 0.037 | 2.39 |
| | α_\odot , pre | 11.066 ± 0.184 | 1.254 ± 0.004 | 2.576 ± 0.006 | 0.090 ± 0.074 | 4409 ± 23 | 1.623 ± 0.022 | 3.94 |
| | α_\odot , post | 11.147 ± 0.177 | 1.250 ± 0.004 | 2.578 ± 0.006 | 0.041 ± 0.083 | 4445 ± 33 | 1.644 ± 0.025 | 3.75 |
| | MR, pre | 10.580 ± 0.043 | 1.262 ± 0.001 | 2.559 ± 0.002 | 0.218 ± 0.062 | 4701 ± 105 | 1.696 ± 0.039 | 3.92 |
| | MR, post | 10.590 ± 0.046 | 1.260 ± 0.001 | 2.559 ± 0.002 | 0.227 ± 0.052 | 4705 ± 122 | 1.698 ± 0.045 | 4.10 |
| | Fid., pre | 13.661 ± 0.229 | 0.608 ± 0.002 | 2.351 ± 0.006 | -0.344 ± 0.072 | 4596 ± 84 | 1.880 ± 0.037 | 2.93 |
| | Fid., post | 13.807 ± 0.231 | 0.605 ± 0.002 | 2.354 ± 0.006 | -0.240 ± 0.099 | 4610 ± 85 | 1.894 ± 0.034 | 2.93 |
| | BG14-2, pre | 13.617 ± 0.228 | 0.618 ± 0.004 | 2.357 ± 0.007 | -0.306 ± 0.074 | 4564 ± 92 | 1.864 ± 0.036 | 2.49 |
| B | BG14-2, post | 13.750 ± 0.242 | 0.614 ± 0.003 | 2.359 ± 0.007 | -0.266 ± 0.111 | 4578 ± 98 | 1.879 ± 0.040 | 2.70 |
| | α_\odot , pre | 13.699 ± 0.239 | 0.607 ± 0.002 | 2.352 ± 0.006 | -0.331 ± 0.066 | 4530 ± 22 | 1.857 ± 0.021 | 2.75 |
| | α_\odot , post | 13.872 ± 0.242 | 0.605 ± 0.002 | 2.356 ± 0.006 | -0.302 ± 0.100 | 4499 ± 51 | 1.856 ± 0.028 | 2.95 |
| | MR, pre | 13.311 ± 0.113 | 0.610 ± 0.001 | 2.342 ± 0.003 | -0.278 ± 0.053 | 4616 ± 64 | 1.865 ± 0.026 | 3.47 |
| | MR, post | 13.332 ± 0.094 | 0.609 ± 0.001 | 2.342 ± 0.003 | -0.148 ± 0.093 | 4615 ± 80 | 1.866 ± 0.032 | 3.74 |
| | Fid., pre | 13.392 ± 0.240 | 0.529 ± 0.002 | 2.281 ± 0.007 | -0.469 ± 0.099 | 4571 ± 74 | 1.854 ± 0.037 | 4.26 |
| | Fid., post | 13.793 ± 0.227 | 0.525 ± 0.002 | 2.291 ± 0.006 | -0.234 ± 0.125 | 4506 ± 82 | 1.855 ± 0.035 | 3.66 |
| | BG14-2, pre | 13.466 ± 0.222 | 0.537 ± 0.003 | 2.291 ± 0.007 | -0.415 ± 0.106 | 4469 ± 102 | 1.819 ± 0.042 | 3.65 |
| C | BG14-2, post | 13.712 ± 0.258 | 0.531 ± 0.003 | 2.293 ± 0.007 | -0.283 ± 0.117 | 4486 ± 83 | 1.842 ± 0.037 | 3.61 |
| | α_\odot , pre | 13.418 ± 0.179 | 0.529 ± 0.001 | 2.282 ± 0.005 | -0.481 ± 0.065 | 4560 ± 23 | 1.851 ± 0.018 | 4.01 |
| | α_\odot , post | 13.812 ± 0.218 | 0.525 ± 0.001 | 2.292 ± 0.006 | -0.294 ± 0.092 | 4404 ± 60 | 1.816 ± 0.026 | 3.64 |
| | MR, pre | 13.045 ± 0.041 | 0.531 ± 0.001 | 2.272 ± 0.001 | -0.353 ± 0.071 | 4504 ± 86 | 1.806 ± 0.033 | 4.52 |
| | MR, post | 13.059 ± 0.054 | 0.530 ± 0.001 | 2.271 ± 0.002 | -0.158 ± 0.118 | 4521 ± 89 | 1.813 ± 0.034 | 4.57 |

For all three stars, the best-fitting models obtained using the oscillations are larger and more massive than the radii and masses derived from the binary solutions. These discrepancies are similar to those found by [Gaulme et al. \(2016\)](#) when using scaling relation. [Thiemeßl et al. \(2018\)](#) finds the same discrepancies when not accounting for the mass, temperature, metallicity or surface effects. The literature contains extensive discussion about how accurate and precise the scaling relations are and some propose corrections to the reference values based on stellar models (e.g. [Guggenberger et al. 2016, 2017](#)). The results here suggest that such corrections might be influenced by inaccuracies in the stellar models themselves, which can be studied in systems that have independent constraints on mass or radius, like the binaries studied here.

It is interesting that the model parameter that changes most when constraining the fits by the dynamical masses and radii is the initial helium abundance Y_0 . The correlation between the mass M and Y_0 is well-known (e.g. [Lebreton & Goupil 2014](#)). The initial helium abundance Y_0 directly affects the mean density of the model and it appears that the increased Y_0 means that the mean densities of the stellar models are much less affected by the inclusion of the orbital constraints. Increasing Y_0 would also make our models more similar to those of [Li et al. \(2018\)](#), who computed models with a fixed enrichment law with $Y_0 = 0.249 + 1.33Z_0$, where Z_0 is the model's initial metal content.

We note again that these results are based on models that neglect gravitational settling and radiative levitation. Gravitational settling could play a role by changing the mean molecular weight and therefore the density throughout the star. However, without an opposing process like rotation or radiative levitation, current im-

Table 5. Comparison of surface effect magnitudes between the different fits and the predictions of [Sonoii et al. \(2015\)](#). Values are 1000 times the fractional surface correction at v_{max} .

| | Star | | |
|--|-------------------|-------------------|-------------------|
| | A | B | C |
| Sonoii et al. , eq. (10) | -5.74 ± 0.74 | -7.86 ± 0.95 | -7.61 ± 0.94 |
| Sonoii et al. , eq. (21) | -5.68 ± 0.60 | -8.47 ± 0.84 | -8.91 ± 0.89 |
| Fid., pre | -3.58 ± 0.72 | -8.18 ± 0.92 | -8.72 ± 0.98 |
| Fid., post | -3.75 ± 0.69 | -6.44 ± 1.58 | -5.19 ± 2.19 |
| α_\odot , pre | -5.50 ± 0.51 | -8.57 ± 0.81 | -8.88 ± 0.80 |
| α_\odot , post | -5.71 ± 0.46 | -8.21 ± 0.79 | -7.12 ± 0.90 |
| BG14-2, pre | -9.94 ± 1.23 | -17.23 ± 3.50 | -18.99 ± 3.63 |
| BG14-2, post | -10.37 ± 1.63 | -14.91 ± 3.69 | -12.07 ± 4.08 |
| MR, pre | -4.07 ± 0.60 | -8.54 ± 0.93 | -9.44 ± 0.97 |
| MR, post | -4.21 ± 0.74 | -7.14 ± 1.49 | -7.30 ± 1.64 |

plementations of gravitational settling make unrealistic predictions about stellar properties on the main sequence. The extent of convective core overshooting is another poorly-constrained process in stellar modelling that would change the stars' mean densities. Thus, there remain several processes that might influence these results, which introduces the possibility that further studies like this one might be able to constrain those same processes.

3.4 Surface effects

The overall scale of the surface corrections is roughly consistent for all the models that use the one-term (cubic) fit by [Ball & Gizon \(2014\)](#). For the two-term (combined) fit, the surface correction is

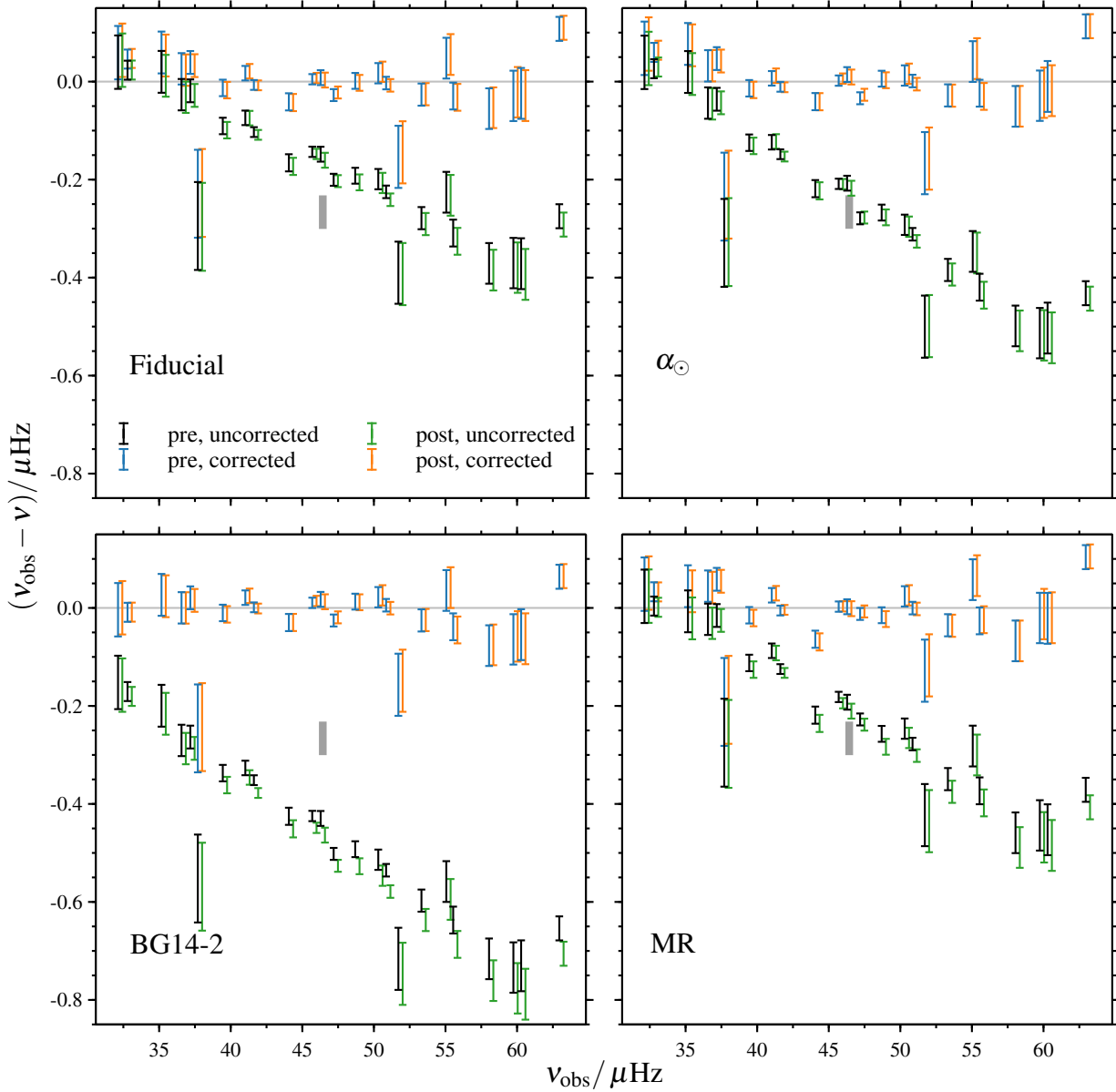


Figure 4. Frequency differences before and after applying a surface correction as a function of observed frequency for best-fitting models of star A (KIC 8410637). The four panels are for the fiducial fit (top left), the fit with solar-calibrated mixing-length (top right), the fit using the two-term surface correction by [Ball & Gizon \(2014\)](#) (bottom left) and the fit using the orbital mass and radius as observable constraints (bottom right). For each fit, we have plotted the frequency difference before (uncorrected) and after correction (corrected) for both the pre- and post-RGB bump models. The post-RGB bump frequencies are shifted right by $0.3 \mu\text{Hz}$ for clarity. The solid grey bar indicates the surface correction predicted by eq. (10) of [Sonoi et al. \(2015\)](#).

somewhat larger in magnitude for all three stars. For stars A and B, the scale of the correction is roughly the same for the pre- and post-bump models, as we expect because the surface effect is determined by near surface properties that are similar in both cases. The surface effects differ between pre- and post-bump models for star C though there the post-bump solution is preferred.

In Table 5 we compare the surface correction at v_{max} with the predictions by [Sonoi et al. \(2015\)](#) computed using the observed data, with uncertainties determined by making random realisations of the observations. We note that the comparison is far from exact. The results in [Sonoi et al. \(2015\)](#) are only for the part of the surface effect

caused by the poor-modelling of the background stellar model and do not incorporate any changes to the dynamics of the oscillations. It does, however, still give some idea of the kind of surface effect that is to be expected. As shown by the figures, the one-term (cubic) correction gives results that are similar to the predicted corrections, whereas the two-term (combined) fit is usually larger.

One of the main results of this article, then, is that fitting models to data using the one-term correction by [Ball & Gizon \(2014\)](#) leads to surface corrections that are similar to those predicted by [Sonoi et al. \(2015\)](#). Though this could only mean that both models are equally wrong, it is at least encouraging that this result is achieved

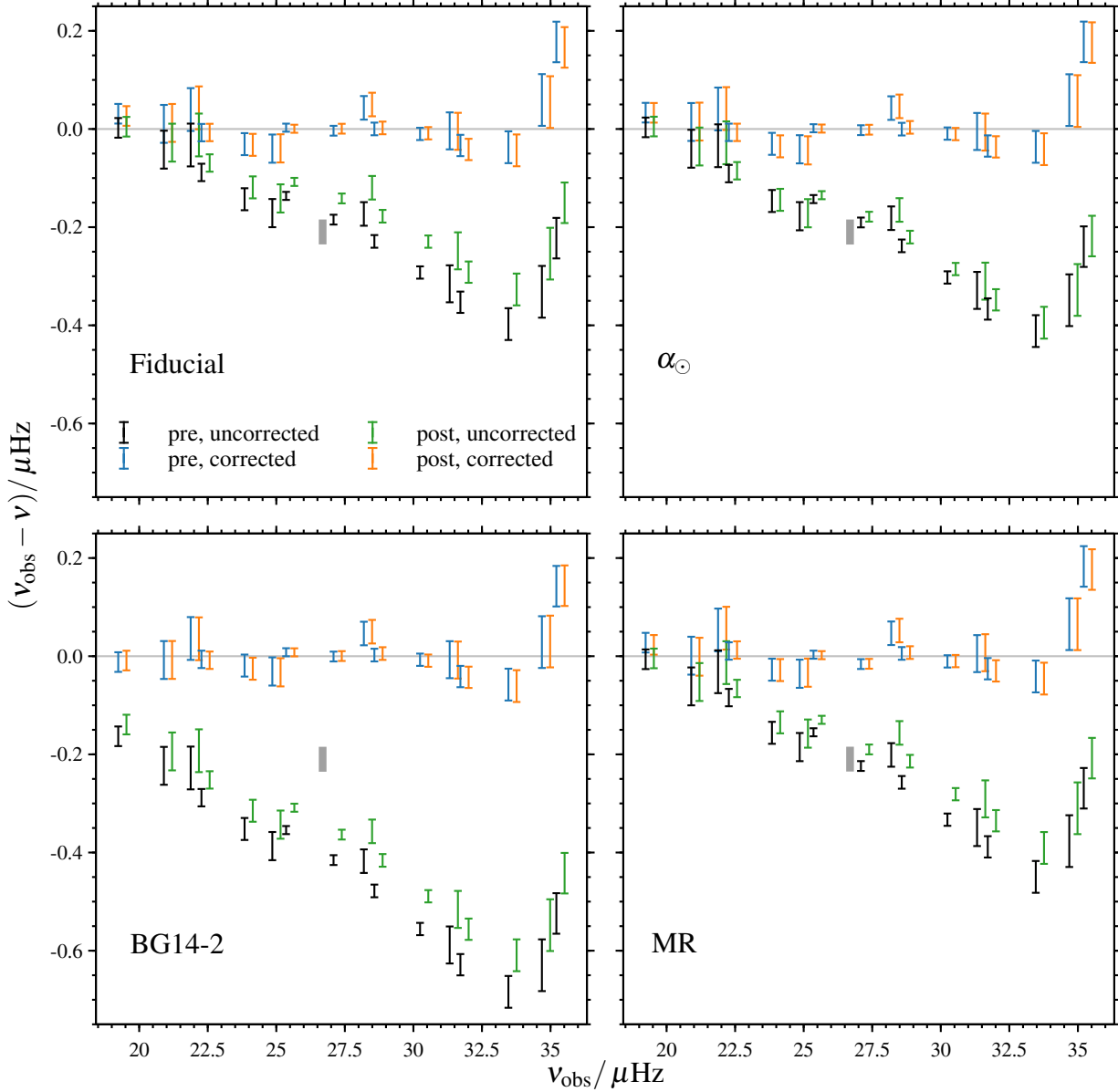


Figure 5. As in Fig. 4 for star B (KIC 9540226).

without additional constraints. The results are also consistent with the surface corrections determined by Pérez Hernández et al. (2016), who found a relative frequency difference $\delta v/v \approx -0.005v_{\max}$ at v_{\max} .

3.5 Mixing-length parameters

Three of our fits for each star allowed the mixing-length parameter α to vary freely. Although there is no obvious trend between the different stars, all the values are larger than the solar-calibrated value $\alpha_{\odot} = 1.66$. Ball & Gizon (2017) also found super-solar mixing-length parameters for their best-fitting models, in that case for fits to subgiants and low-luminosity red giants ($3.5 \lesssim \log g \lesssim 3.8$), as did Li et al. (2018) for their sample of six eclipsing binaries with similar

Table 6. Mixing-length parameters determined by interpolating in the results of Magic et al. (2015). The second column gives the predicted mixing-length parameter relative to the solar value in the grid. The third column is the same value multiplied by our solar-calibrated value of $\alpha_{\odot} = 1.66$, for comparison with Table 3.

| Star | $\alpha/\alpha_{\odot, \text{STAGGER}}$ | $\times \alpha_{\odot, \text{MESA}}$ |
|------|---|--------------------------------------|
| A | 0.959 ± 0.009 | 1.591 ± 0.015 |
| B | 0.951 ± 0.008 | 1.579 ± 0.014 |
| C | 0.951 ± 0.008 | 1.578 ± 0.013 |

parameters to ours (and including stars A and B). Similarly, Tayar et al. (2017) found that, to reconcile temperatures from spectroscopy

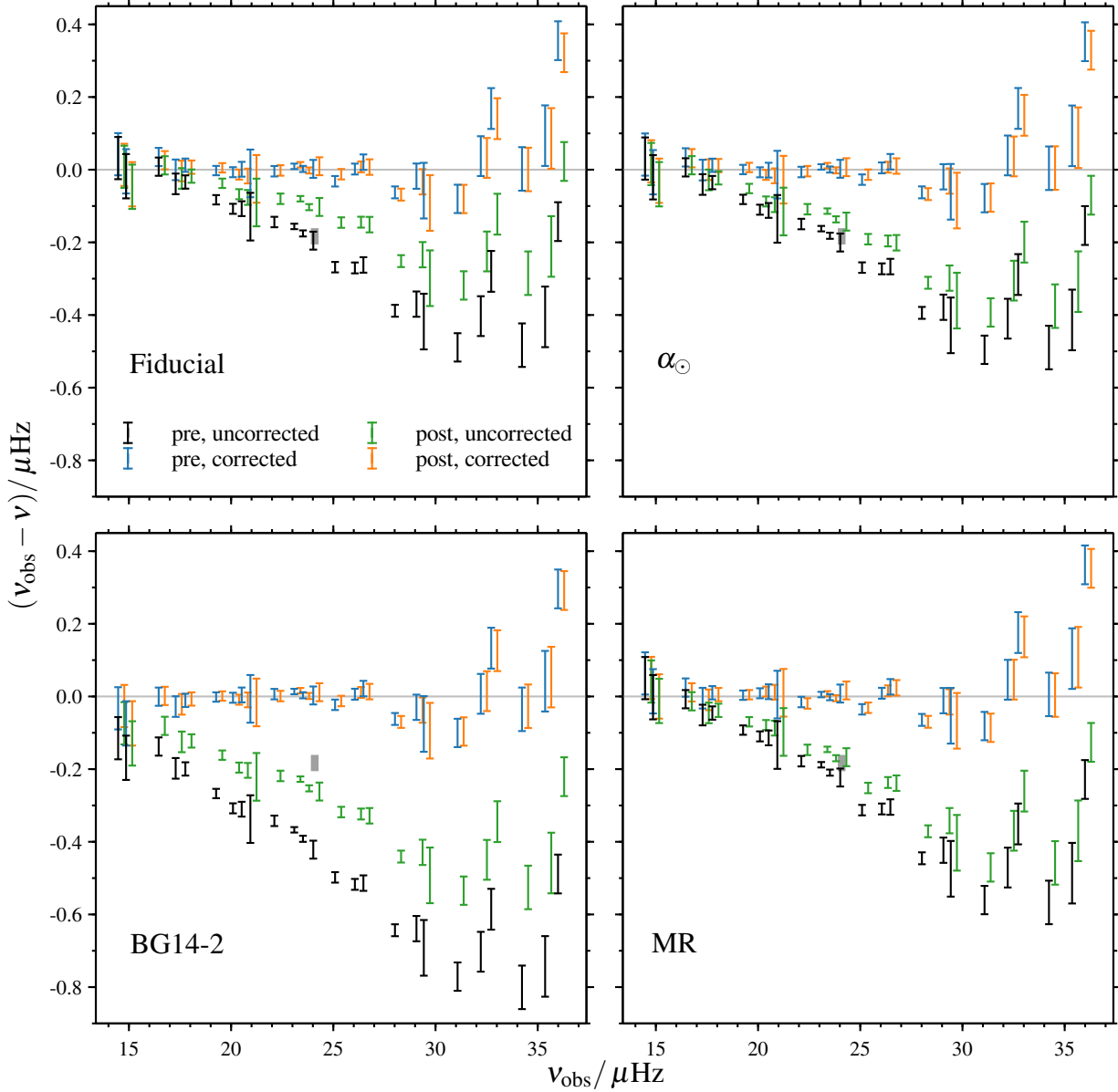


Figure 6. As in Fig. 4 for star C (KIC 5640750).

and evolutionary tracks, they too would need to increase the mixing-length parameters of their models above the solar-calibrated values.

Like [Ball & Gizon \(2017\)](#), we have compared our best-fitting mixing-length parameters with the predictions of [Magic et al. \(2015\)](#), which are based on calibrations of mixing-length envelope models to three-dimensional radiation hydrodynamics simulations from the STAGGER code. We generated 10^5 values of v_{\max} , T_{eff} and $[\text{Fe}/\text{H}]$ and used them to interpolate in their data for mixing-length parameters calibrated to the entropy jump at the bottom boundary of the simulation. In Table 6, we list the means and standard deviations determined for each star relative to the solar-calibrated value in the simulation data. We also give the value multiplied by the solar-calibrated mixing-length parameter for the MESA models presented here.

Table 6 shows that the simulations support smaller mixing-length parameters than our best-fitting stellar models. In fact, they suggest that the mixing-length parameter should be less than the solar-calibrated value. Combined with the results of [Ball & Gizon \(2017\)](#), [Li et al. \(2018\)](#) and [Tayar et al. \(2017\)](#), there appears to be a growing tension with the predictions of hydrodynamics simulations, or at least those of [Magic et al. \(2015\)](#). It is not clear what the source of such tension might be. One possibility is the choice of atmospheric model, which is known to affect the mixing-length parameter. In that case, the implication would be that the Eddington approximation gives a poor atmospheric model for evolved stars. This could be tested by incorporating the atmospheric models of the hydrodynamics simulations, which could be performed using the

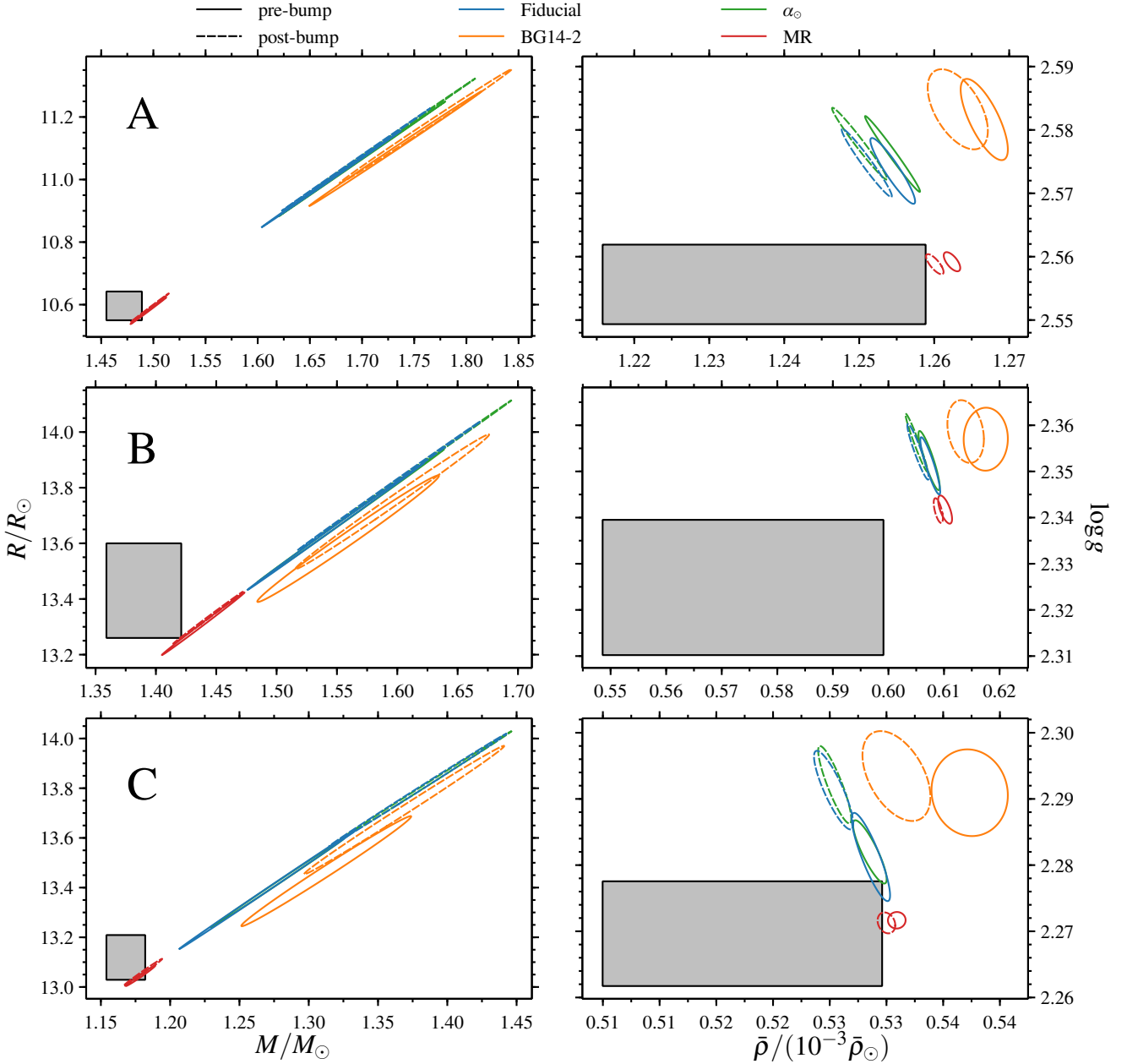


Figure 7. Plot showing the masses M versus radii R (left) and mean densities $\bar{\rho}$ versus surface gravities $\log g$ (right) for the various fits, compared to the values derived from the orbital solutions (grey boxes). From top to bottom, the plots show the results for stars A, B and C (KIC 8410637, KIC 9540226 and KIC 5640750). The blue, orange, green and red ellipses correspond to the fiducial fits, the fits with the two-term correction by Ball & Gizon (2014), the fits with a solar-calibrated mixing-length parameter, and the fits with the mass and radius constraints from the orbital solutions. In each case, the parameters of the best fitting models before and after the RGB bump are shown with solid (pre-bump) or dashed (post-bump) lines. Note that in some cases the pre- and post-bump solutions are indistinguishable.

method set out by Trampedach et al. (2014), though this is beyond the scope of the present work.

4 CONCLUSION

The mode suppression method we have presented gives unbiased results at the cost of greater uncertainties in the inferred parameters. With this level of uncertainty, however, we still find that the one-term (cubic) surface correction by Ball & Gizon (2014) leads to

a correction that agrees with the prediction by Sonoi et al. (2015). This is broadly true for the solutions before or after the RGB bump and whether or not the dynamical masses and radii are included as constraints. The two-term (combined) correction by Ball & Gizon (2014) appears to lead to somewhat larger surface corrections. Overall, the surface effects in the three stars are robust, with shifts of about 0.1–0.3 μHz at v_{max} for all three stars across all the fits that use the cubic correction.

Without constraining them to agree, the stellar models lead to significantly discrepant masses and radii compared with the orbital

solutions. The masses and radii are still incorrect even when the mixing-length parameter is fixed at the solar-calibrated value. The discrepancy in all the stars is similar to the roughly 15 and 5 per cent in mass and radius found by [Gaulme et al. \(2016\)](#) and [Themeßl et al. \(2018\)](#) when the scaling relations are not corrected for the effects of mass, effective temperature, metallicity or surface effects. The initial helium abundance Y_0 changes the most when the masses and radii are constrained to match the dynamical values, which suggests that the difference might be caused by the composition profile of the stellar models through processes like gravitational settling and rotation, which have been ignored here.

While our mode suppression method has allowed us to infer stellar properties and surface corrections for these three stars, it would clearly be better to be able to exploit the full set of observed modes. As it is, we do not make use of any information about the stellar core that is contained in the mixed modes and constrain processes like core overshooting on the main sequence (e.g. [Montalbán et al. 2013](#); [Lagarde et al. 2016](#)). Nevertheless, it presents a step forward in establishing that the surface effect in RGB stars manifests itself in a way similar to main-sequence stars and in line with our expectations from hydrodynamic simulations.

ACKNOWLEDGEMENTS

WHB acknowledges the support of the UK Science and Technology Facilities Council (STFC). The research leading to the presented results has received funding from the European Research Council under the European Community's Seventh Framework Programme (FP7/2007-2013) / ERC grant agreement no 338251 (StellarAges).

REFERENCES

- Angulo, C., Arnould, M., Rayet, M., et al. 1999, *Nuclear Physics A*, 656, 3
 Appourchaux, T., Antia, H. M., Ball, W. H., et al. 2015, *A&A*, 582, A25
 Auvergne, M., Bodin, P., Boissard, L., et al. 2009, *A&A*, 506, 411
 Ball, W. H. 2017, in *European Physical Journal Web of Conferences*, Vol. 160, *European Physical Journal Web of Conferences*, 02001
 Ball, W. H. & Gizon, L. 2014, *A&A*, 568, A123
 Ball, W. H. & Gizon, L. 2017, *A&A*, 600, A128
 Beck, P. G., Bedding, T. R., Mosser, B., & et al. 2011, *Science*, 332, 205
 Beck, P. G., Hambleton, K., Vos, J., et al. 2014, *A&A*, 564, A36
 Beck, P. G., Montalbán, J., Kallinger, T., & et al. 2012, *Nature*, 481, 55
 Bedding, T. R., Mosser, B., Huber, D., & et al. 2011, *Nature*, 471, 608
 Belkacem, K., Marques, J. P., Goupil, M. J., et al. 2015a, *A&A*, 579, A31
 Belkacem, K., Marques, J. P., Goupil, M. J., et al. 2015b, *A&A*, 579, A30
 Bellinger, E. P., Angelou, G. C., Hekker, S., et al. 2017, in *European Physical Journal Web of Conferences*, Vol. 160, *European Physical Journal Web of Conferences*, 05003
 Böhm-Vitense, E. 1958, *Z. Astrophys.*, 46, 108
 Borucki, W. J., Koch, D., Basri, G., et al. 2010, *Science*, 327, 977
 Brogaard, K., Jessen-Hansen, J., Handberg, R., et al. 2016, *Astronomische Nachrichten*, 337, 793
 Brown, T. M., Gilliland, R. L., Noyes, R. W., & Ramsey, L. W. 1991, *ApJ*, 368, 599
 Caughlan, G. R. & Fowler, W. A. 1988, *Atomic Data and Nuclear Data Tables*, 40, 283
 Christensen-Dalsgaard, J. 2008, *Ap&SS*, 316, 113
 Corsaro, E., De Ridder, J., & García, R. A. 2015, *A&A*, 579, A83
 Cox, J. P. & Giuli, R. T. 1968, *Principles of stellar structure* (Gordon and Breach, New York)
 Creevey, O. L., Metcalfe, T. S., Schultheis, M., et al. 2017, *A&A*, 601, A67
 Deheuvels, S., García, R. A., Chaplin, W. J., et al. 2012, *ApJ*, 756, 19
 Ferguson, J. W., Alexander, D. R., Allard, F., et al. 2005, *ApJ*, 623, 585

- Frandsen, S., Lehmann, H., Hekker, S., et al. 2013, *A&A*, 556, A138
 Gaulme, P., Jackiewicz, J., Appourchaux, T., & Mosser, B. 2014, *ApJ*, 785, 5
 Gaulme, P., McKeever, J., Jackiewicz, J., et al. 2016, *ApJ*, 832, 121
 Gaulme, P., McKeever, J., Rawls, M. L., et al. 2013, *ApJ*, 767, 82
 Grevesse, N. & Sauval, A. J. 1998, *Space Sci. Rev.*, 85, 161
 Guggenberger, E., Hekker, S., Angelou, G. C., Basu, S., & Bellinger, E. P. 2017, *MNRAS*, 470, 2069
 Guggenberger, E., Hekker, S., Basu, S., & Bellinger, E. 2016, *MNRAS*, 460, 4277
 Hekker, S. & Christensen-Dalsgaard, J. 2017, *A&ARv*, 25, 1
 Hekker, S., Debosscher, J., Huber, D., et al. 2010, *ApJ*, 713, L187
 Igelesias, C. A. & Rogers, F. J. 1996, *ApJ*, 464, 943
 Imbriani, G., Costantini, H., Formicola, A., et al. 2005, *European Physical Journal A*, 25, 455
 Kjeldsen, H. & Bedding, T. R. 1995, *A&A*, 293, 87
 Kunz, R., Fey, M., Jaeger, M., et al. 2002, *ApJ*, 567, 643
 Lagarde, N., Bossini, D., Miglio, A., Vrad, M., & Mosser, B. 2016, *MNRAS*, 457, L59
 Lebreton, Y. & Goupil, M. J. 2014, *A&A*, 569, A21
 Li, T., Bedding, T. R., Huber, D., et al. 2018, *MNRAS*, 475, 981
 Magic, Z., Weiss, A., & Asplund, M. 2015, *A&A*, 573, A89
 Marques, J. P., Goupil, M. J., Lebreton, Y., et al. 2013, *A&A*, 549, A74
 Miglio, A., Chaplin, W. J., Farmer, R., et al. 2014, *ApJ*, 784, L3
 Miglio, A., Chiappini, C., Morel, T., et al. 2013, *MNRAS*, 429, 423
 Montalbán, J., Miglio, A., Noels, A., et al. 2013, *ApJ*, 766, 118
 Mosser, B., Benomar, O., Belkacem, K., et al. 2014, *A&A*, 572, L5
 Nelder, J. A. & Mead, R. 1965, *The Computer Journal*, 7, 308
 Paxton, B., Bildsten, L., Dotter, A., et al. 2011, *ApJS*, 192, 3
 Paxton, B., Cantiello, M., Arras, P., et al. 2013, *ApJS*, 208, 4
 Paxton, B., Marchant, P., Schwab, J., et al. 2015, *ApJS*, 220, 15
 Pérez Hernández, F., García, R. A., Corsaro, E., Triana, S. A., & De Ridder, J. 2016, *A&A*, 591, A99
 Planck Collaboration, Ade, P. A. R., Aghanim, N., et al. 2016, *A&A*, 594, A13
 Reese, D. R., Chaplin, W. J., Davies, G. R., et al. 2016, *A&A*, 592, A14
 Silva Aguirre, V., Lund, M., Antia, H. M., et al. 2017, *ApJ*, 835, 173
 Sonoi, T., Samadi, R., Belkacem, K., et al. 2015, *A&A*, 583, A112
 Tayar, J., Somers, G., Pinsonneault, M. H., et al. 2017, *ApJ*, 840, 17
 Themeßl, N., Hekker, S., Southworth, J., et al. 2018, *MNRAS*, accepted
 Trampedach, R., Stein, R. F., Christensen-Dalsgaard, J., Nordlund, Å., & Asplund, M. 2014, *MNRAS*, 442, 805
 White, T. R., Benomar, O., Silva Aguirre, V., et al. 2017, *A&A*, 601, A82

APPENDIX A: SOURCE CODE FOR SUPPRESSING CORE GRAVITY MODES

Here, we detail the modifications to MESA's Fortran source (revision 9575) necessary to reproduce the g-mode suppression described in Sec. 2.3. All the modifications are applied when the stellar model data is stored for ADIPLS, in the subroutine `store_model_for_adipls` on lines 231–340 of the file `$MESA_DIR/star/astero/src/adipls_support.f`. Here, `$MESA_DIR` is the environment variable specifying MESA's top-level directory.

First, we declare a new set of variables at the beginning of the subroutine by inserting the following code at line 247.

```
1 integer :: k
2 real(dp) :: dlnP_dlnr, dlnrho_dlnr
```

Then, we insert the following code at line 312 (in the unmodified file) to loop over the stellar model and perform the calculations described in Sec. 2.3.

```
1 ! suppress oscillations in the core by modifying AA directly
2 if (dbg) write(*,*) 'modifying aa'
3 do k=2,nn-1
```

```

4  if ((x(k) < 0.4) .and. (aa(4,k) > 0)) then
5    dlnP_dlnr = -aa(3,k)*aa(2,k)
6    dlnrho_dlnr = -aa(2,k)-aa(4,k)
7    aa(4,k) = 0d0 ! A = 0
8    aa(2,k) = aa(2,k)*aa(3,k) ! multiply Vg by Gamma_1
9    aa(3,k) = dlnP_dlnr/dlnrho_dlnr ! Gamma_1 = dlnP/dlnrho
10   aa(2,k) = aa(2,k)/aa(3,k) ! divide to get new Vg
11   end if
12 end do
13 aa(4,1) = 2*aa(4,2)-aa(4,3)
14 if (dbg) write(*,*) 'done modifying aa'

```

Line 4 selects those points in the core that are convectively stable. The hardcoded fractional radius $x < 0.4$ can be any value in the convective envelope. Lines 5 and 6 recover $d\ln P/d\ln r$ and $d\ln \rho/d\ln r$ from the existing model data. Line 7 assigns $N^2 = 0$ and lines 8–10 reassign the adiabatic index Γ_1 to its new value given by eq. (1). Line 13 assigns N^2 at the central point by linear interpolation.